Inorganic Chemistry

Article

pubs.acs.org/IC

Hydrogenous Zintl Phase $Ba_3Si_4H_x$ (x = 1−2): Transforming Si_4 "Butterfly" Anions into Tetrahedral Moieties

Verina F. Kranak,[†] Daryn E. Benson,[‡] Lukas Wollmann,[§] Milad Mesgar,[§] Samrand Shafeie,[†] Jekabs Grins,[†] and Ulrich Häussermann*[,†]

[†]Department of Materials and Environmental Chemistry, Stockholm University, SE-10691 Stockholm, Sweden

[‡]Department of Physics, Arizona State University, Tempe, Arizona 85287-1504, United States

[§]Department of Chemistry, Arizona State University, Tempe, Arizona 85287-1604, United States

Supporting Information

ABSTRACT: The hydride $Ba_3Si_4H_x$ (x = 1−2) was prepared by sintering the Zintl phase Ba_3Si_4, which contains Si_4^{6-} butterfly-shaped polyanions, in a hydrogen atmosphere at pressures of 10−20 bar and temperatures of around 300 °C. Initial structural analysis using powder neutron and X-ray diffraction data suggested that $Ba_3Si_4H_x$ adopts the $Ba_3Ge_4C_2$ type [space group $I4/mcm$ (No. 140), $a \approx 8.44$ Å, $c \approx 11.95$ Å, $Z = 8$] where Ba atoms form a three-dimensional array of corner-condensed octahedra, which are centered by H atoms. Tetrahedron-shaped Si_4 polyanions complete a perovskite-like arrangement. Thus, hydride formation is accompanied by oxidation of the butterfly polyanion, but the model with the composition Ba_3Si_4H is not charge-balanced. First-principles computations revealed an alternative structural scenario for $Ba_3Si_4H_x$, which is based on filling pyramidal Ba_5 interstices in Ba_3Si_4. The limiting composition is $x = 2$ [space group $P4_2/mmm$ (No. 136), $a \approx 8.4066$ Å, $c \approx 12.9186$ Å, $Z = 8$], and for $x > 1$, Si atoms also adopt tetrahedron-shaped polyanions. Transmission electron microscopy investigations showed that $Ba_3Si_4H_x$ is heavily disordered in the c direction. Most plausible is to assume that $Ba_3Si_4H_x$ has a variable H content (x = 1−2) and corresponds to a random intergrowth of P- and I-type structure blocks. In either form, $Ba_3Si_4H_x$ is classified as an interstitial hydride. Polyanionic hydrides in which H is covalently attached to Si remain elusive.

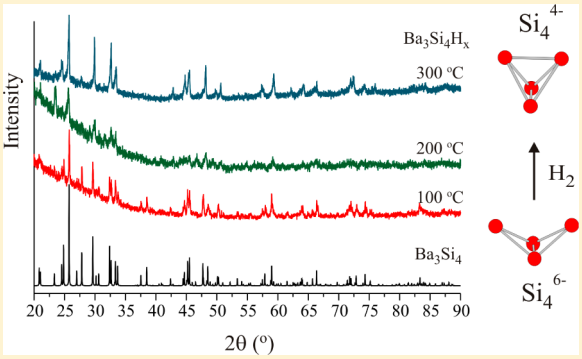

I. INTRODUCTION

Like many intermetallic compounds, Zintl phases constituted of an active metal (alkali, alkaline earth, or rare earth) and a more electronegative p-block metal or semimetal can react with H to form hydrides.[1−3] However, the rather high ionicity of Zintl phases makes such hydrides peculiar. As a characteristic feature of Zintl phases, atoms of the electronegative component appear reduced and may form polyanionic structures to achieve an octet. H takes an ambivalent role and can be incorporated in two principal ways: either hydridic, where H is exclusively coordinated by active metals (interstitial hydrides), or as part of the polyanion, where it acts as a covalently bonded ligand (polyanionic hydrides).[2,3] The H content of hydrogenous Zintl phases is comparatively low; however, the chemical structures and physical properties of Zintl phases can change profoundly upon H incorporation. This provides interesting prospects for fundamental inorganic chemistry and materials science.

Rather well investigated are ternary compounds MTrTt formed from M = Ca−Ba, Tr = Al−In, and Tt = Si−Sn.[4−7] Their structures derive from the simple AlB_2 type with Tr and Tt atoms commonly distributed over the site of the B atoms, forming hexagon-planar layers. Systems MTrTt represent charge-imbalanced (electron excess) Zintl phases and are metallic conductors (frequently even superconductors). Hydrogenation induces a transition into semiconducting hydrides MTrTtH, where H is bonded to Tr and thus part of the polyanion.[8] Well-studied examples of interstitial hydrides from Zintl phase hydrogenations are various Ca−Si−H phases.[9−11] H incorporation in CaSi leads to oxidation of the zigzag-chain Si polyanion. The oxidation manifests itself in the formation of Si−Si interchain bonds and thus new polyanionic moieties in the phases $CaSiH_1$ and $CaSiH_{1.2}$.[11] For Ca_5Si_3 and Ca_2Si, H incorporation leads to the formation of amorphous hydrogenous phases.[12,13] Amorphization and/or H-induced oxidative decompositions are frequently observed upon hydrogenation of Zintl phases.[3,14]

The compositional range of hydrogenous Zintl phases is not yet explored. Also it remains unclear what factors govern the formation of polyanionic hydrides as opposed to interstitial ones. Polyanionic hydrides have been especially observed with Al and Ga. Will it be possible to extend those to group 14 elements and add H to, e.g., a Si polyanion? To explore these

Special Issue: To Honor the Memory of Prof. John D. Corbett

Received: June 16, 2014
Published: September 23, 2014

   dx.doi.org/10.1021/ic501421u | Inorg. Chem. 2015, 54, 756−764

fundamental issues further, we investigated the hydrogenation behavior of Ba_3Si_4. This well-established Zintl phase was already reported in 1969[15] and recently reinvestigated by Aydemir et al.[16] It contains peculiar "butterfly" polyanions Si_4^{6-} consisting of two different kinds of Si atoms: two two-bonded Si^{2-} defining the "butterfly wings" and two three-bonded Si^{-} defining the "butterfly abdomen" (Figure 1). Although

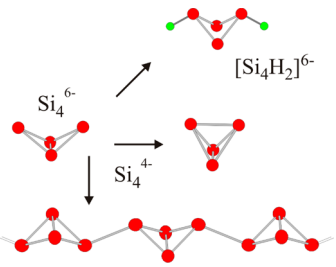

Figure 1. Butterfly anion Si_4^{6-} in Ba_3Si_4 and envisioned changes upon the formation of charge-balanced hydrogenous $Ba_3Si_4H_2$.

charge-balanced, Ba_3Si_4 shows a metallike temperature dependence of the resistivity and has been classified as poor metal.[16] A range of scenarios can be envisioned in the case that hydrogenation leads to phases $Ba_3Si_4H_x$. This is sketched in Figure 1. H may be incorporated interstitially and oxidizes two-bonded Si^{2-} to three-bonded Si^{-}. As a result, either bond formation within the butterfly entities may be induced (yielding tetrahedral polyanions Si_4^{4-}) or butterfly entities may polymerize to one-dimensional chains. Both scenarios would be charge-balanced for a composition $x = 2$. The polymerization of butterfly anions (accompanied by the loss of the abdomen bond) is observed in polymorphic Ba_3Ge_4 when the high-temperature form, which adopts the Ba_3Si_4 structure, is cooled below 357 °C.[17] Alternatively, one could think of the formation of a polyanionic hydride, where H is added to the butterfly anion (or its polymeric derivative) upon Si−Si bond opening. In summary, Ba_3Si_4 appears to be a versatile system for studying the fundamental aspects of hydrogenous Zintl phases. However, the sketched scenarios assume first that hydrogenous phases can be obtained and second that the composition Ba:Si = 3:4 is maintained.

II. EXPERIMENTAL SECTION

Synthesis. All steps of the synthesis and sample preparation were carried out in an Ar-filled glovebox. Ba (99.99% purity) and Si (99.999% purity) were purchased from Sigma-Aldrich. Ba_3Si_4 was prepared by arc-melting stoichiometric amounts of the pure elements. Powdered Ba_3Si_4 was pressed into a pellet (with a mass of 100−200 mg), which was placed in a corundum crucible. The crucible was loaded into a stainless steel autoclave, which was evacuated and then pressurized with hydrogen or deuterium gas. The hydride $Ba_3Si_4H_x$ (x = 1−2) was obtained at conditions of 300 °C and 10 bar of H_2 for 40 h. For the deuteride analogue, reaction conditions were 300 °C and 20 bar of D_2 for 40 h. To examine the desorption behavior, pellets of $Ba_3Si_4H_x$ (with a mass of about 50 mg) were placed in a fused-silica tube in an Ar-filled glovebox. Once removed from the glovebox, the fused-silica tube was evacuated and held under dynamic vacuum conditions (10^{-3} Torr), while the sample was heated for 18 h at the desired temperature. Both Ba_3Si_4 and $Ba_3Si_4H_x$ have a gray color and decompose slowly when exposed to moist air.

Diffraction Experiments. Initial structural analysis was performed by powder X-ray diffraction (PXRD) using a Bruker D8 diffractometer, which was fitted with an incident beam Ge monochromator (transmission geometry; Cu $K\alpha_1$ radiation). Powder samples were measured in 0.3 mm capillaries. Time-of-flight powder neutron diffraction data were collected on the powder neutron diffractometer at the Lujan Neutron Scattering Center at Los Alamos National Laboratory. The sample (about 3.0 g) was loaded into a V container and measured at room temperature for 12 h. High-energy PXRD measurements were carried out at the beamline P02.1 at PETRA III, DESY (Hamburg, Germany). This beamline operates at a fixed energy of approximately 60 keV. The wavelength was determined to be 0.20727(6) Å. Samples were enclosed in 0.5 mm glass capillaries, and 30 two-dimensional diffraction images, each obtained through the accumulation of 20 frames with an exposure time of 1 s/frame, were collected with a PerkinElmer amorphous Si area detector (XRD1621) placed at 329 mm from the sample. The two-dimensional diffraction images were then integrated into a linear scattering signal with the software *Fit2D* and averaged.[18] Rietveld analysis of the PXRD data was performed using the program package *FULLPROF*.[19]

Electron Microcopy Investigations. Samples for electron microscopy investigations were ground in a mortar, and the resulting fine crystallites were supported on holey-carbon-coated copper grids in the glovebox. Transfer of the sample onto the sample holder and into the electron microscope was done under normal air conditions. Transmission electron microscopy (TEM) studies were carried out in a JEOL JEM-2100 F microscope operated at 200 kV. The three-dimensional reciprocal lattice was constructed using the rotational electron diffraction (RED) technique.[20] Data were collected using a single-tilt tomography holder that operates under the control of *RED* software.[21] The three-dimensional image was constructed from 1307 frames.

Computational Modeling. The theoretical calculations of the electronic structure, total energies, and structural optimizations were performed using the first-principles all-electron projector augmented wave method[22,23] within the Vienna ab Initio Simulation Package.[24,25] Exchange-correlation effects were treated within the generalized gradient approximation via the Perdew−Burke−Ernzerhof parametrization.[26,27] The structures considered were relaxed to ambient pressure with respect to the lattice parameters and atomic positions. Forces on atomic positions were converged to better than 10^{-3} eV/Å. Valence electrons were treated as $5s^25p^66s^2$, $3s^23p^2$, and $1s^1$ for Ba, Si, and H, respectively. The electronic integration over the Brillouin zone was performed on a Monkhorst−Pack grid of special k-points of size 6 × 6 × 4 (4 × 4 × 3 during relaxation).[28] The decomposition of the density of states (DOS) into atomic contributions was based on spheres with radii of 1.98, 1.11, and 0.53 Å for Ba, Si, and H, respectively. The plane-wave basis set was terminated at a kinetic energy cutoff of 350 eV. Formation energies were assessed according to $\Delta E(Ba_3Si_4H_x) = E(Ba_3Si_4H_x) - x/2E(H_2)$. The H_2 molecule was treated in a box with the size 10 × 10 × 10 Å.

III. RESULTS AND DISCUSSION

Hydrogenation Behavior of Ba_3Si_4: Synthesis of $Ba_3Si_4H_x$. Ba_3Si_4 was sintered in a hydrogen atmosphere at various conditions in order to explore the temperature, pressure, and time aspects of the hydrogenation reaction. Figure 2 shows selected PXRD patterns of reaction products obtained at temperatures between 100 and 400 °C while the pressure and annealing time were kept constant (at 30 bar and 40 h, respectively). At temperatures below 200 °C, the hydrogenation reaction has no significant rate. At 200 °C, a broadening of reflections and a loss of intensity indicate partial amorphization. The pattern at 300 °C suggests the formation of a crystalline hydrogenous phase. We note that it is not unusual for Zintl phases to initially degrade into an amorphous material upon hydrogenation, from which a hydrogenous phase crystallizes at higher temperatures. This phenomenon is even observed when metal-atom arrangements in the Zintl phase and hydride are very similar.[6] At 400 °C, the pattern appears again changed. More but broader reflections indicate the formation of

dx.doi.org/10.1021/ic501421u | Inorg. Chem. 2015, 54, 756−764

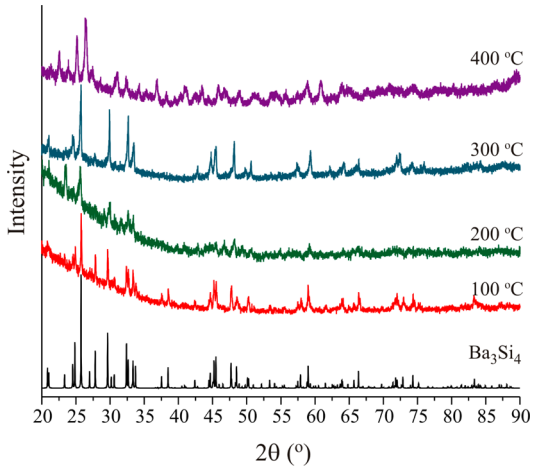

Figure 2. PXRD patterns (Cu Kα_1) of products from the hydrogenation of Ba_3Si_4 at 30 bar, 40 h, and over a range of 100–400 °C.

a second, more complex structured phase or H-induced decomposition into (amorphous) BaH_2 and a (hydrogenous) Si-richer phase.

Varying the annealing time (and keeping the temperature and pressure constant at 300 °C and 30 bar, respectively) shows the formation of the initial hydrogenous phase after several hours; however, after long-term sintering (for 96 h), the diffraction pattern appears changed again (Figure S1a in the Supporting Information, SI). This pattern is different from that obtained at 400 °C after 40 h of sintering (cf. Figure 2). Increasing the pressure from 30 to 50 bar leads to an amorphous product (Figure S1b in the SI). We conclude that Ba_3Si_4 shows a complicated hydrogenation behavior, possibly involving the formation of multiple hydrogenous phases, crystalline and amorphous. In this work, we will focus on the initial phase, in the following termed $Ba_3Si_4H_x$, for which we then diligently tried to establish optimum synthesis conditions. Samples were obtained best crystalline when using 300 °C, 40 h, and 10–20 bar, and those conditions were also applied to synthesize the deuteride analogue. Yet, we realized that synthesis runs were difficult to reproduce. Powder patterns of products from identical synthesis conditions showed slight differences in the intensity distribution and, more or less pronounced, the presence of what seemed to be extra reflections from impurities. The PXRD patterns of one $Ba_3Si_4H_x$ and two $Ba_3Si_4D_x$ samples are compiled in Figure 3a. Those samples are termed "H", "D1", and "D2" in the following. For structure elucidation, especially the D1 and D2 samples were used.

The thermal stability of $Ba_3Si_4H_x$ was investigated by performing desorption experiments in a dynamic vacuum (10^{-3} Torr). Decomposition was not observed until 400 °C. At 500 °C, a mixture of Ba_3Si_4 and an amorphous phase was obtained (Figure S2 in the SI). Raman and IR spectra of $Ba_3Si_4H_x$ are essentially featureless, which indicates that this phase is a metal.

Initial Structure Analysis of $Ba_3Si_4H_x$. When impurity reflections are excluded, the PXRD patterns of $Ba_3Si_4H_x$ could be indexed to a tetragonal body-centered lattice with unit cell parameters very similar to those of the primitive tetragonal cell of Ba_3Si_4 ($a \approx 8.44$ Å; $c \approx 11.95$ Å). These parameters bear also great resemblance to those of the body-centered $Ba_3Si_4C_2$

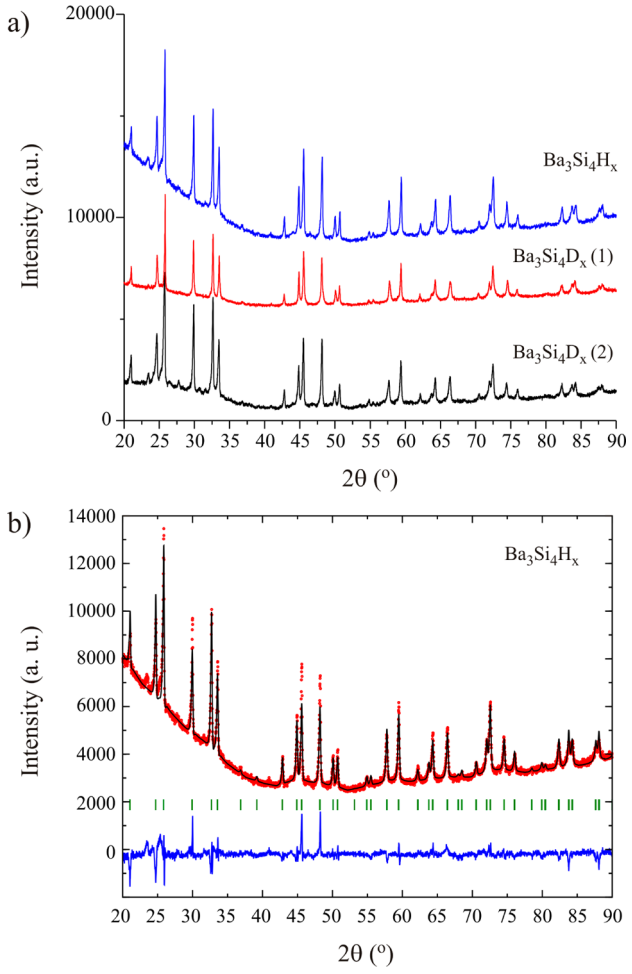

Figure 3. (a) PXRD patterns (Cu Kα_1) of the samples "H", "D1", and "D2" obtained from Ba_3Si_4 at 300 °C and 10 bar of H_2/40 h ("H") and 20 bar of D_2/40 h ("D1" and "D2"). (b) Rietveld fit of the *I*-Ba_3Si_4H model (tetragonal body centered) to the "H" diffraction data (Cu Kα_1).

structure,[29] suggesting a close relationship. In the $Ba_3Si_4C_2$ structure ($Ba_3Ge_4C_2$ type), Ba atoms form a three-dimensional array of mutually rotated corner-condensed octahedra (similar to O atoms in perovskites, in particular the $GdFeO_3$ structure) and tetrahedral Si_4 units take the positions of the large metal atoms.[30] Acetylide C_2 dumbbell moieties center Ba_6 octahedra. Black $Ba_3Si_4C_2$ is a semiconducting Zintl phase, with Ba^{2+} balancing the charges of C_2^{2-} and Si_4^{4-}.[29] The situation is not exactly transferable to a hydride. Only one H atom (or rather a H^- ion) may center a Ba_6 octahedron, yielding charge-imbalanced Ba_3Si_4H. The structures of *I*-centered Ba_3Si_4 ("*I*-Ba_3Si_4" with empty octahedra) and Ba_3Si_4H ("*I*-Ba_3Si_4H") were subsequently optimized by density functional theory (DFT) calculations. The structure parameters for the equilibrium volumes are reported in Table 1. Table 2 lists relevant interatomic distances. It is seen that the unit cell volume of hypothetical *I*-Ba_3Si_4 is about 3.5% larger than that of the primitive ground-state structure ("*P*-Ba_3Si_4"), whose structure parameters are also contained in Table 1. The larger unit cell is exclusively attributable to a more elongated *c* axis. With H incorporated, the unit cell volume of *I*-Ba_3Si_4 shrinks and the volume of *I*-Ba_3Si_4H corresponds roughly to that of *P*-Ba_3Si_4; however, the *c*/*a* ratio is significantly larger (by almost 5%). Although the calculated powder pattern of the DFT-optimized

dx.doi.org/10.1021/ic501421u | *Inorg. Chem.* 2015, 54, 756–764

Table 1. Structure Parameters of Primitive and Body-Centered Tetragonal Forms of Ba_3Si_4 and Derived Hydrides Obtained from First-Principles Calculations[a]

	P-Ba_3Si_4 (exp)	*P*-Ba_3Si_4 (calc)	*P*-$Ba_3Si_4H_2$		*I*-Ba_3Si_4	*I*-Ba_3Si_4H
a (Å)	8.5233	8.5819	8.4066		8.5494	8.4374
c (Å)	11.8322	11.9559	12.9186		12.4507	12.3044
V (Å^3)	859.57	880.54	912.96		910.04	875.94
	(*x*, *y*, *z*)				(*x*, *y*, *z*)	
Ba1 (4g)	0.3352, 0.6649, 0	0.3360, 0.6640, 0	0.8172, 0.1828, 0	Ba1 (4a)	0, 0, 0.25	0, 0, 0.25
Ba2 (4e)	0, 0, 0.1696	0, 0, 0.1690	0, 0, 0.3184	Ba2 (8h)	0.1814, 0.6814, 0	0.1819, 0.6819, 0
Ba3 (4d)	0, 0.5, 0.25	0, 0.5 0.25	0, 0.5, 0.25			
Si1 (8i)	0.0995, 0.3001, 0	0.1007, 0.3007, 0	0.2120, 0.4201, 0	Si (16l)	0.1032, 0.6032, 0.1842	0.1061, 0.6061, 0.1848
Si2 (8j)	0.2992, 0.2992, 0.1460	0.3006, 0.3006, 0.1443	0.1795, 0.1795, 0.0957			
H (8j)			0.7546, 0.7546, 0.6919	H (4c)		0, 0, 0

[a]For *P*-Ba_3Si_4, experimental values according to ref 16 are given for comparison.

Table 2. Interatomic Distances for Primitive and Body-Centered Tetragonal Forms of Ba_3Si_4 and Derived Hydrides Obtained from First-Principles Calculations[a]

d (Å)	*P*-Ba_3Si_4 (exp)	*P*-Ba_3Si_4 (calc)	*P*-$Ba_3Si_4H_2$	*I*-Ba_3Si_4	*I*-Ba_3Si_4H
Ba1−H			2.62 (2×)		3.08 (2×)
Ba2−H			2.92 (2×)		3.09 (2×)
Ba3−H			3.07 (4×)		
Ba1−Si	3.58 (4×), 3.70 (2×), 3.71 (2×)	3.56 (4×), 3.70 (2×), 3.73 (2×)	3.29 (4×), 3.35 (2×), 3.87 (2×)	3.60 (8×)	3.53 (8×)
Ba2−Si	3.26 (2×), 3.36 (4×), 3.62 (2×)	3.27 (2×), 3.36 (4×), 3.62 (2×)	3.44 (4×), 3.58 (2×), 3.97 (2×)	3.41 (4×), 3.47 (2×), 4.04 (2×)	3.39 (4×), 3.40 (2×), 3.98 (2×)
Ba3−Si	3.30 (4×), 3.52 (2×)	3.32 (4×), 3.52 (2×)	3.68 (4×), 3.75 (4×)		
Si−H			2.85		
Si1−Si	2.42, 2.43 (2×)	2.41, 2.41 (2×)	2.39 (2×), 2.47	2.41 (2×), 2.50	2.40 (2×), 2.53
Si2−Si	2.43 (2×), 3.45	2.41 (2×), 3.41	2.39 (2×), 2.47		

[a]For *P*-Ba_3Si_4, experimental values according to ref 16 are given for comparison.

structure of *I*-Ba_3Si_4H displays great similarities with the experimental patterns, there are significant deviations. Attempts to fit this structure model to the PXRD data were unsatisfactory (Figure 3b). Noticeable is also the fact that the refined *c* parameter (11.95 Å) is 0.35 Å (~3%) smaller, which cannot be explained by DFT shortcomings because the experimental structure of *P*-Ba_3Si_4 is excellently reproduced by DFT optimization (cf. Table 1). We conclude that the model structure for $Ba_3Si_4H_x$ established in analogy to $Ba_3Si_4C_2$ has issues. Before addressing these in more detail, we describe the relationship between the *I*-Ba_3Si_4H model and *P*-Ba_3Si_4 (Figure 4).

The structure of *P*-Ba_3Si_4 [space group $P4_2/mnm$ (No. 136)] is depicted in Figure 4a and consists of three kinds of Ba atoms and two types of Si atoms. As was already mentioned, the latter atoms form a butterfly Si_4^{6-} polyanion. Ba2 and Ba3 atoms on sites 4e and 4d, respectively, are arranged into a corrugated 4^4 (square) net, which is alternately capped from above and below by (apical) Ba1 atoms (on site 4g) to yield a corrugated layer of tetragonal pyramids in the *ab* plane. Those layers are connected by sharing apical Ba1 atoms along the *c* direction. Cavities provided by this framework of edge- and corner-condensed Ba pyramids are centered round the site 4g ($^1/_4$, $^3/_4$, 0) and occupied by the butterfly polyanions. As pointed out by Aydemir et al., the Ba_3Si_4 structure relates to the $TiAl_3$ structure, where Al atoms form square-planar layers and Ti atoms correspond to the centers of butterfly polyanions.[16] This is shown in Figure 4b. When the *P*-Ba_3Si_4 structure is idealized as a $TiAl_3$-type arrangement, the close relationship to *I*-Ba_3Si_4H becomes immediately clear. A simple shift of atoms situated on the planes (100) in the $TiAl_3$ structure by $^1/_2$ *a* will yield the perovskite structure. In *I*-Ba_3Si_4H (Figure 4c), Ba_6 octahedra are additionally mutually rotated and, importantly, butterfly anions are converted into tetrahedra.

The Si−Si distances in the DFT-optimized structures of *I*-Ba_3Si_4H and H-free *I*-Ba_3Si_4 are very similar, 2.40−2.41 and 2.50−2.53 Å, despite their significant difference in the unit cell volume (cf. Table 2). The Si−Si distances in the carbide $Ba_3Si_4C_2$ are somewhat shorter (2.38 and 2.47 Å).[29] Thus, it seems that the charge imbalance of *I*-Ba_3Si_4 and *I*-Ba_3Si_4H is not strongly reflected in the intratetrahedral distances. Also, the Si−Si distances in the tetrahedral Si_4 moieties of *I*-Ba_3Si_4, *I*-Ba_3Si_4H, and $Ba_3Si_4C_2$ compare well with those of the binary Zintl phases ASi (A = Na−Cs) and $BaSi_2$. However, Si_4 tetrahedra in the latter are more regular. Molecular compounds Si_4R_4 with an uncharged Si_4 tetrahedron display shorter Si−Si distances (around 2.32 Å).[31]

Computational Modeling of $Ba_3Si_4H_x$ Structures. *I*-Ba_3Si_4H appears as a reasonable structure model for $Ba_3Si_4H_x$. First, there is a close relationship to the initial *P*-Ba_3Si_4 structure. Second, the structural change of the polyanion (from butterfly to tetrahedron) is in line with the expected oxidation upon interstitial hydride formation, although *I*-Ba_3Si_4H would not be charge-balanced. However, as shown in Figure 3b, the model cannot be fit satisfactorily to the experimental PXRD patterns. Because the *I*-Ba_3Si_4H structure does not provide any apparent location for further H atoms, we investigated the possibility of H incorporation in the *P*-Ba_3Si_4 structure. Here the most obvious location is the center of the Ba_5 pyramids. We created model structures by simply occupying Ba_5 pyramids in Ba_3Si_4 with H atoms and relaxed them subsequently by DFT calculations. For those simulations,

dx.doi.org/10.1021/ic501421u | Inorg. Chem. 2015, 54, 756−764

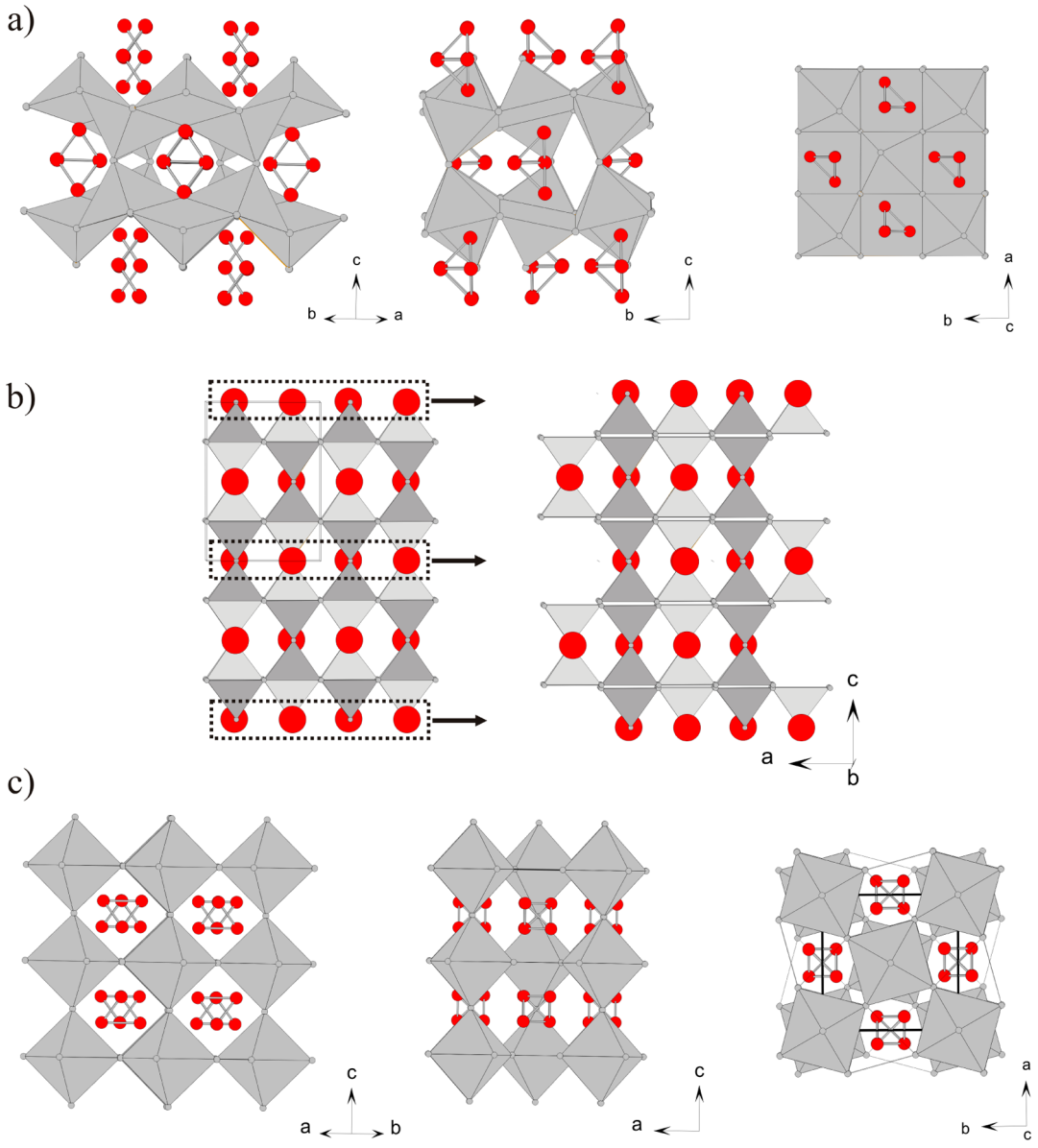

Figure 4. (a) Tetragonal primitive crystal structure of Ba_3Si_4 (*P*-Ba_3Si_4) projected along the [110], [100], and [001] directions. Ba atoms are arranged as corrugated 4^4 (square) nets (best seen in the [001] projection), which are alternately capped above and below to yield a layer of (distorted) square pyramids. Pyramid layers are connected along the [001] direction. Cages host Si_4 butterfly moieties. Ba atoms/polyhedra are shown in gray and Si atoms/clusters in red. (b) Left: Idealized view of *P*-Ba_3Si_4 corresponding to the $TiAl_3$ structure. Ba/Al atoms are represented as gray atoms/polyhedra, and large red spheres represent Si_4 clusters/Ti atoms. Right: Slip of atoms on planes (100) by $t = (^1/_2a, 0, 0)$ transforming the primitive structure into a body-centered tetragonal one. Ba atoms are arranged as an array of corner-sharing octahedra. (c) Tetragonal body-centered crystal structure of Ba_3Si_4H (*I*-Ba_3Si_4H) projected along the [110], [100], and [001] directions. Color code as in (a).

we considered the unit cell of Ba_3Si_4 containing eight pyramids ($Z = 4$), which accommodates the compositions $Ba_{12}Si_{16}H_n$ with $n = 1-8$. Possible symmetry relations were not considered, and consequently the starting models had symmetry *P*1. Figure 5 summarizes the salient results of DFT structure optimization; more details are given as SI. Importantly, for $n = 1-4$, butterfly polyanions are essentially maintained. H attaches to the wings via a rather long Si−H bond (1.65 Å) while at the same time being coordinated by the 5 Ba atoms of a pyramid. Note that the Si−H bond length in silanes is typically around 1.5 Å. As expected, the abdomen Si−Si bond is elongated (cf. Figure 1). Such hydrides could be regarded as polyanionic hydrides. For $n = 4$, mixed scenarios with Si_4 tetrahedra and Si_4H and Si_4H_2 butterfly anions occur. Interestingly, for $n = 8$, Si polyanions correspond to tetrahedra with Si−Si distances closely relating to those in $Ba_3Si_4C_2$ (2.39 and 2.47 Å). The *P*1 relaxed structure for $Ba_{12}Si_{16}H_8$ ($Ba_3Si_4H_2$) deviated only marginally from the tetragonal $P4_2/mnm$ symmetry, with H atoms occupying site 8i. The structure parameters for $Ba_3Si_4H_2$ in space group $P4_2/mnm$ ("*P*-$Ba_3Si_4H_2$") are included in Table 1.

Figure 6 compares the electronic DOS of the structure models. *P*-Ba_3Si_4 represents a charge-balanced Zintl phase. Its DOS is characterized by a pronounced (i.e., steep) pseudogap at the Fermi level (Figure 6a). Our result for *P*-Ba_3Si_4 is virtually identical with the previously reported DOS by Aydemir et al.[16] Si s bands are weakly dispersed and centered around −6 eV (three bands) and −10.5 eV (one band, not shown in Figure 6a) below the Fermi level. The valence band

dx.doi.org/10.1021/ic501421u | *Inorg. Chem.* 2015, 54, 756−764

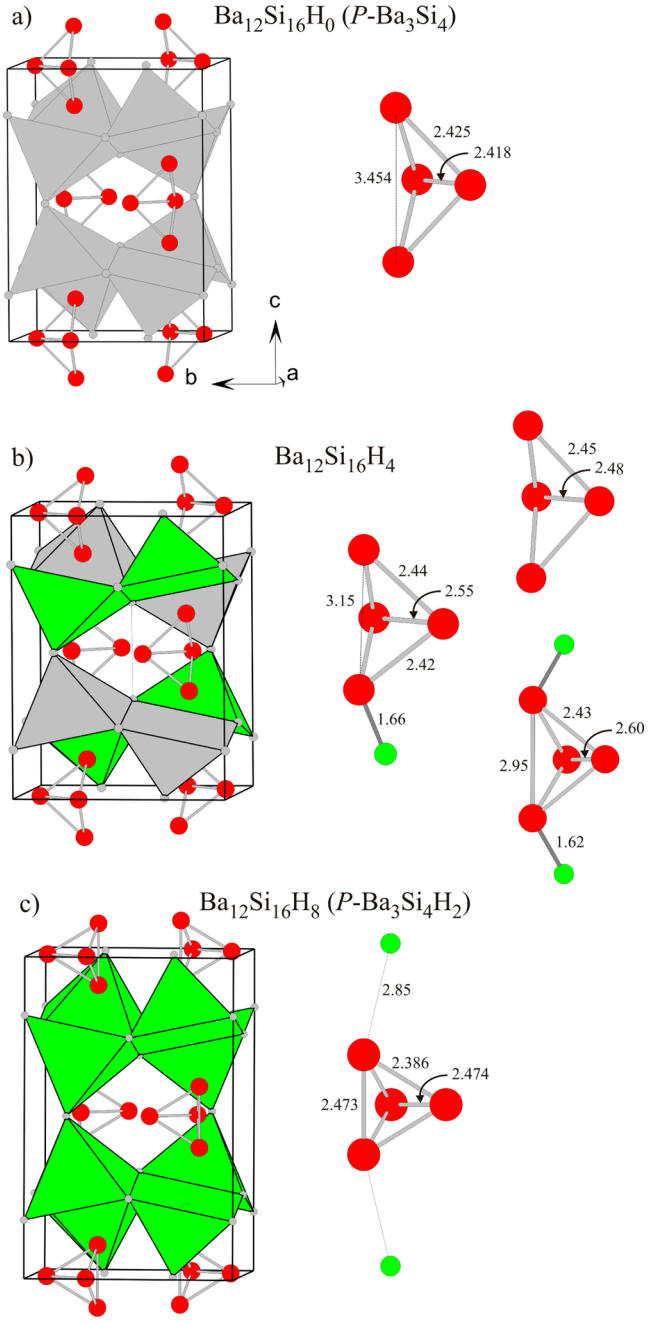

Figure 5. Selected results from the computational modeling of $Ba_{12}Si_{16}H_n$ (n = 0–8). (a) Unit cell of $Ba_{12}Si_{16}H_0$ (P-Ba_3Si_4). The Ba_5 tetragonal pyramids are highlighted (gray). The associated butterfly Si polyanion is drawn in red. Si–Si interatomic distances (in Å) are indicated. (b) Unit cell of a selected structure for $Ba_{12}Si_{16}H_4$. H-centered Ba_5 pyramids are indicated in green. There are 70 possibilities to distribute four H atoms in eight pyramids, and for n = 4, various polyanions Si_4, Si_4H, and Si_4H_2 are found. Some of them are shown. (c) Unit cell of $Ba_{12}Si_{16}H_8$ (P-$Ba_3Si_4H_2$) with all Ba_5 pyramids filled and associated tetrahedral Si_4 polyanion.

from −3.5 eV up to the Fermi level is composed of Si p and Ba d states. In the DOS of charge-imbalanced I-Ba_3Si_4 (Figure 6b), the position of the pseudogap conforms with the electron count of the tetrahedral polyanion Si_4^{4-}, and the Fermi level is located above. It is also noticeable that the three Si s bands around −6 eV that are separated for P-Ba_3Si_4 merge into a "t_2" band for I-Ba_3Si_4. In the DOS of P-derived $Ba_{12}Si_{16}H_4$ and I-Ba_3Si_4H (Figure 6c,d), the relative positions of the gaps still correspond to the electron counts of Si_4^{6-} and Si_4^{4-}, respectively, and the Fermi level is then shifted above and below. For P-$Ba_{12}Si_{16}H_4$, H 1s states mix with the Si s bands, which expresses the Si–H interaction (bond). For I-Ba_3Si_4H, H 1s states mix into the bottom of the valence band. Finally, P-$Ba_3Si_4H_2$ corresponds to a charge-balanced Zintl phase (Figure 6e). In contrast with P-Ba_3Si_4, a proper band gap with a size of 0.4 eV has opened at the Fermi level. The shape of the DOS below the Fermi level, which is determined by the electronic structure of Si_4^{4-}, is very similar to that of I-Ba_3Si_4H.

Next we compare the formation energies $\Delta E(Ba_{12}Si_{16}H_n) = E(Ba_{12}Si_{16}H_n) - n/2E(H_2)$ with respect to the total energy of P-Ba_3Si_4. The results are displayed in Figure 7. This figure also includes the values obtained for I-derived $Ba_{12}Si_{16}H_n$ (n = 0, 1, 4), i.e., the energies of one unit cell of I-Ba_3Si_4 with none, one, and all Ba_6 octahedra H-centered. In Figure 7, positive values imply an energetically unfavorable situation against P-Ba_3Si_4. This is clearly the case for I-Ba_3Si_4, which, however, stabilizes largely upon H incorporation. The incorporation of H in the pyramids of P-Ba_3Si_4 is also favorable but not to the same extent. For n = 4, I-Ba_3Si_4H has the lowest formation energy. However, it is important to note that P-derived $Ba_{12}Si_{16}H_4$ experiences sizable stabilization through configurational entropy ($S_{config} = R \ln \Omega$) from the possibility of arranging four H atoms in eight pyramids (Ω = 70; S_{config} = 35.3 J/K cell). At a synthesis temperature of 300 °C, $T\Delta S_{config}$ amounts to about 0.21 eV/cell. Thus, the Gibbs energies of formation for P-derived $Ba_{12}Si_{16}H_4$ and I-Ba_3Si_4H may be rather similar. Finally, we note that the end member of the P series, P-$Ba_3Si_4H_2$ (cf. Figure 5c), appears surprisingly stable. We emphasize that the formation energies in Figure 7 refer to a 0 K situation; that is, contributions from, e.g., zero-point energy and vibrational entropy, have been neglected. Yet, the result should capture the energetics of the $Ba_3Si_4H_x$ system quite well. An initial formation of P-$Ba_3Si_4H_x$ may be kinetically favored because hydride formation is accompanied by only a minor rearrangement of the metal atoms.

The result from the computational simulations opens up for new scenarios concerning the structural behavior of $Ba_3Si_4H_x$. It is reasonable to assume a homogeneity range $\sim 1 < x < \sim 2$. Also, because of the close relationship of P- and I-type structures, it is reasonable to assume that P- and I-type slabs with variable H content are intergrown at the unit cell level. For either structure, Si would adopt a tetrahedron-shaped polyanion when $\sim 1 < x < \sim 2$.

Structural Analysis of $Ba_3Si_4H_x$ Revisited. A TEM study of crystals of the D1 sample strongly corroborates the presence of structural disorder. The three-dimensional reconstruction of the reciprocal space was performed by the RED technique, where a crystal is finely tilted, not specified to any zone axis, and electron diffraction (ED) patterns are continuously taken.[20] ED patterns along high-symmetry zone axes (shown in Figure S3 in the SI) showed massive violation of the I centering and pronounced diffuse scattering along the c^* direction characteristic of stacking disorder.

Although conventional Rietveld refinement will not be capable of modeling disordered intergrowth structures, we performed a multiphase refinement of the D1 sample, including three phases, P-Ba_3Si_4 (starting material), I-Ba_3Si_4H, and P-$Ba_3Si_4H_2$. The result is shown in Figure 8 for the synchrotron diffraction data, where the effects of absorption are minimized. At first sight, the fit appears satisfactorily; especially, all Bragg

dx.doi.org/10.1021/ic501421u | Inorg. Chem. 2015, 54, 756–764

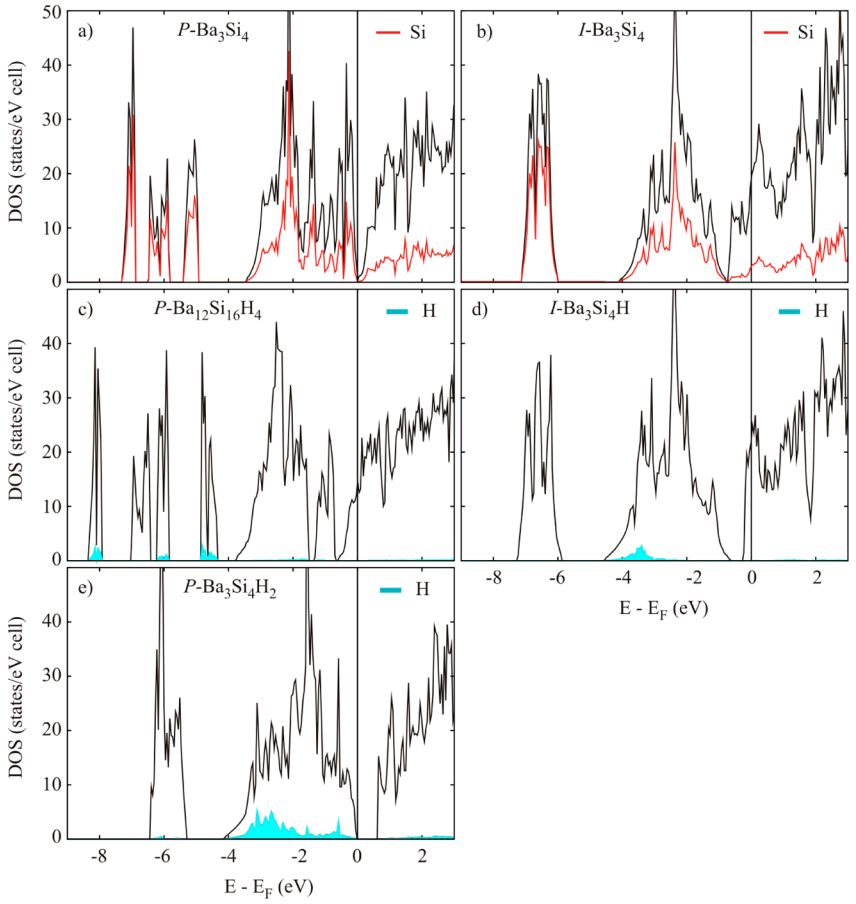

Figure 6. Electronic DOS for *P*-Ba_3Si_4 (a), *I*-Ba_3Si_4 (b), $Ba_{12}Si_{16}H_4$ as shown in Figure 5b (c), *I*-Ba_3Si_4H (d), and *P*-$Ba_3Si_4H_2$ as shown in Figure 5c (e). The Fermi level is indicated by a horizontal line.

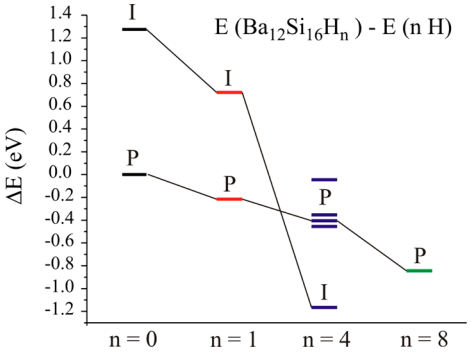

Figure 7. Formation energies $\Delta E = E(Ba_{12}Si_{16}H_n) - n/2E(H_2)$ of *P*- and *I*-derived arrangements of $Ba_{12}Si_{16}H_n$ (n = 0, 1, 4, 8) with respect to the total energy of *P*-Ba_3Si_4. For $Ba_{12}Si_{16}H_4$, the energy of four configurations is given.

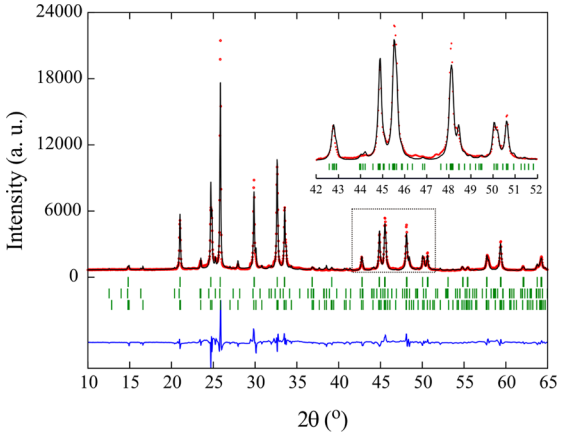

Figure 8. Multiphase Rietveld fit to the synchrotron PXRD data of the "D1" sample. The considered phases were *I*-Ba_3Si_4H, *P*-$Ba_3Si_4H_2$, and *P*-Ba_3Si_4 (R_F = 5.2, 22, and 13%; χ^2 = 11.4).

peaks in the pattern are now accounted for. The phase fractions obtained are roughly 50% *I*-Ba_3Si_4H and 50% *P* phases. The *a* lattice parameter of the three phases is very similar (~8.42 Å) and matches the calculated parameter for *I*-Ba_3Si_4H and *P*-$Ba_3Si_4H_2$ [but not the *a* parameter of the starting material *P*-Ba_3Si_4 (~8.52 Å; cf. Table 1)]. Roughly, in this Rietveld refinement, the ill-defined *c* lattice parameter of $Ba_3Si_4H_x$ (as a result from the structural disorder) is handled by fitting three phases with slightly different *c*/*a* ratios.

The inadequacy of modeling microscopic intergrowth as a macroscopic phase mixture is then very apparent in the peak-shape misfits (inset in Figure 8). Although refined atomic position parameters are similar to the calculated model structures, they are highly inaccurate. Explicit refinement results are presented as SI for the neutron diffraction data of the D2 sample (Figure S4 and Table S1). It is not very meaningful to discuss them, apart from the fact that the models for *I*-Ba_3Si_4H and *P*-$Ba_3Si_4H_2$ were clearly associated with H(D) occupancy.

dx.doi.org/10.1021/ic501421u | *Inorg. Chem.* 2015, 54, 756−764

The atomic pair distribution function (PDF) extracted from the neutron scattering data of the D2 sample is shown in Figure 9 for r up to 4 Å. Data were processed with the *PDFgetN*

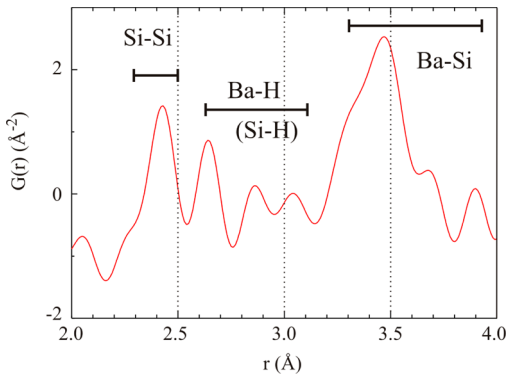

Figure 9. PDF obtained from the Fourier transform of $Ba_3Si_4D_x$ neutron scattering data (D2 sample), truncated at Q_{max} = 35 Å^{-1}. Distance ranges according to Table 2 are indicated.

software[32] and terminated at Q_{max} = 35 Å^{-1}. The peak around 2.4 Å has to correspond to nearest-neighbor Si−Si distances. According to Table 2, the peaks next, at around 2.65, 2.85, and 3.05 Å, are then associated with the Ba−H and Si−H distances. Nearest-neighbor Ba−Si distances start off at around 3.2 Å and stretch to 4 Å, thus overlapping with next-nearest-neighbor Si−Si distances. The peaks in the PDF are broad because they account for a range of similar, not resolved, interatomic distances, which is typical of disordered materials. Although the quality of the PDF of our D2 sample only allows for qualitative analysis, proper modeling of PDF data—or, more generally, total scattering data—will be the key to obtaining explicit and reliable information on the local structure in disordered $Ba_3Si_4H_x$ in the future. The impressive power (and complexity) of total scattering data analysis in probing the local structure of disordered and also amorphous materials has been reviewed recently.[33,34] In our case, this first requires the collection of new high-Q neutron scattering data, which contain the diffuse scattering part with sufficient statistics. Second, data should be preferably modeled with a reverse Monte Carlo (RMC) method (e.g., RMCProfile),[35] which allows fitting of the total scattering data in both reciprocal space and real space. Starting atomic configurations for RMC modeling will be naturally based on the computationally relaxed P and I models with compositions $Ba_{12}Si_{16}H_n$ (n = 0−8). RMC simulation boxes usually contain several thousands of atoms. Variable H(D) concentrations can be probed and consequences to the ratio of P- and I-type slabs and their intergrowth studied.

IV. CONCLUSION

H incorporation in Zintl phases can lead to interstitial or polyanionic hydrides. In the former case, H acts hydridic, formally oxidizing the polyanion, and structural consequences may be rationalized by the Zintl concept. In the latter case, H acts as a covalently bonded ligand in the polyanion. Hydrogenation of Ba_3Si_4 leads to the interstital hydride $Ba_3Si_4H_x$, where butterfly-shaped Si_4^{6-} polyanions are oxidized into tetrahedron-shaped moieties. $Ba_3Si_4H_x$ is structurally disordered, and in the course of this work, the precise H content x and details of the local structure could not be resolved. From a combination of computational modeling and standard crystallographic techniques for structure refinement, it was concluded that the H content of $Ba_3Si_4H_x$ is variable (x = 1−2) and that its structure corresponds to a random intergrowth of hydrogenous building blocks derived from the starting material (P-type) and from the $Ba_3Ge_4C_2$ structuree (I-type). The hydrogenation behavior of Ba_3Si_4 is complex, and the here-presented phase is most likely only one of several hydrogenous phases. For obtaining more detailed information on the local structure of disordered $Ba_3Si_4H_x$, neutron total scattering data suitable for modeling by RMC techniques should be collected. RMC modeling of the total scattering data would also allow insight into the presence of polyanionic species Si_4H_n in $Ba_3Si_4H_x$. First-principles computations indicate that for compositions $x \sim 1$ such species with rather long Si−H bonds may occur, but there is yet no experimental evidence.

■ ASSOCIATED CONTENT

Supporting Information

PXRD patterns of products from the hydrogenation of Ba_3Si_4 at 300 °C and variable time and pressure conditions (Figure S1), PXRD patterns of $Ba_3Si_4H_x$ after being exposed to dynamic vacuum for 18 h at various temperatures (Figure S2), ED patterns for the $Ba_3Si_4H_x$ "D1" sample (Figure S3), and results of the Rietveld refinement of neutron powder diffraction data of the $Ba_3Si_4H_x$ "D2" sample (Figure S4 and Table S1), and compilation of structural parameters for selected computationally relaxed configurations $Ba_{12}Si_{16}H_n$ (Table S2). This material is available free of charge via the Internet at http://pubs.acs.org.

■ AUTHOR INFORMATION

Corresponding Author

*E-mail: Ulrich.Haussermann@mmk.su.se.

Notes

The authors declare no competing financial interest.

■ ACKNOWLEDGMENTS

This work was supported by the U.S. National Science Foundation (Contract DMR-0638826) and the Swedish Research Council [Contracts 2010-4827 and 2011-6512 (Röntgen-Ångström Cluster program)]. The research made use of the Manuel Lujan, Jr. Neutron Scattering Center at Los Alamos National Laboratory, which is funded by the Department of Energy's Office of Basic Energy Sciences. Los Alamos National Laboratory is operated by Los Alamos National Security, LLC, under DOE Contract DE-AC52-06NA25396. Additionally we acknowledge PETRA III, DESY, for provision of synchrotron radiation beamtime and thank Dr. Hanns-Peter Liermann for assistance in using beamline P02.1.

■ REFERENCES

(1) Gingl, F.; Vogt, T.; Akiba, E. *J. Alloys Compd.* **2000**, *306*, 127−132.
(2) Häussermann, U. *Z. Kristallogr.* **2008**, *223*, 628−635.
(3) Häussermann, U.; Kranak, V. F.; Puhakainen, K. Hydrogenous Zintl Phases: Interstitial Versus Polyanionic Hydrides. In *Zintl Phases: Principles and Recent Developments*; Fässler, T. F., Ed.; Structure and Bonding Series; Springer: Berlin, Germany, 2011; Vol. *139*, pp 143−161.
(4) Björling, T.; Noréus, D.; Jansson, K.; Andersson, M.; Leonova, E.; Edén, M.; Hålenius, U.; Häussermann, U. *Angew. Chem., Int. Ed.* **2005**, *44*, 7269−7273.

(5) Evans, M. J.; Holland, G. P.; Garcia-Garcia, J. F.; Häussermann, U. *J. Am. Chem. Soc.* **2008**, *130*, 12139−12147.
(6) Evans, M. J.; Kranak, V. F.; Holland, G. P.; Daemen, L. L.; Proffen, T.; Lee, M. H.; Sankey, O. F.; Häussermann, U. *Inorg. Chem.* **2009**, *48*, 5602−5605.
(7) Kranak, V. F.; Evans, M. J.; Daemen, L. L.; Proffen, T.; Lee, M. H.; Sankey, O. F.; Häussermann, U. *Solid State Sci.* **2009**, *11*, 1847−1853.
(8) Lee, M. H.; Björling, T.; Utsumi, T.; Moser, D.; Noréus, D.; Bull, D.; Hauback, B.; Sankey, O. F.; Häussermann, U. *Phys. Rev. B* **2008**, *78*, 195209.
(9) Aoki, M.; Ohba, N.; Noritake, T.; Towata, S. *Appl. Phys. Lett.* **2004**, *85*, 387−388.
(10) Ohba, N.; Aoki, M.; Noritake, T.; Miwa, K.; Towata, S. *Phys. Rev. B* **2005**, *72*, 075104.
(11) Wu, H.; Zhou, W.; Udovic, T. J.; Rush, J. J.; Yildirim, T. *Phys. Rev. B* **2006**, *74*, 224101.
(12) Wu, H.; Zhou, W.; Udovic, T. J.; Rush, J. J. *Chem. Mater.* **2007**, *19*, 329−334.
(13) Wu, H.; Zhou, W.; Udovic, T. J.; Rush, J. J.; Yildirim, T. *Chem. Phys. Lett.* **2007**, *460*, 432−437.
(14) Wenderoth, P.; Kohlmann, H. *Inorg. Chem.* **2013**, *52*, 10525−10531.
(15) Eisenmannm, B.; Janzon, K. H.; Schafer, H.; Weiss, A. *Z. Naturforsch. B* **1969**, *24*, 457.
(16) Aydemir, U.; et al. *Z. Anorg. Allg. Chem.* **2008**, *634*, 1651−1661.
(17) Zürcher, F.; Nesper, R. *Angew. Chem., Int. Ed.* **1998**, *37*, 3314−3318.
(18) Hammersley, A. P.; Svensson, S. O.; Hanfland, M.; Fitch, A. N.; Häusermann, D. *High Pressure Res.* **1996**, *14*, 235−248.
(19) Rodriguez-Carvajal, J. *FullProf 2.k*, version 5.20; ILL: Grenoble, France, 2011. Rodríguez-Carvajal, J. *Abstracts of the Satellite Meeting on Powder Diffraction of the XV IUCr Congress*; Wiley: New York, 1990; p 127.
(20) Zhang, D. L.; Oleynikov, P.; Hovmöller, S.; Zou, X. D. *Z. Kristallogr.* **2010**, *225*, 94−102.
(21) Wan, W.; Sun, J. L.; Su, J.; Hovmöller, S.; Zou, X. D. *J. Appl. Crystallogr.* **2013**, *46*, 1863−1873.
(22) Blöchl, P. E. *Phys. Rev. B* **1994**, *50*, 17953−17979.
(23) Kresse, G.; Joubert, D. *Phys. Rev. B* **1999**, *59*, 1758−1775.
(24) Kresse, G.; Hafner, J. *Phys. Rev. B* **1993**, *48*, 13115−13118.
(25) Kresse, G.; Furthmüller, J. *Comput. Mater. Sci.* **1996**, *6*, 15−50.
(26) Perdew, J. P.; Burke, K.; Ernzerhof, M. *Phys. Rev. Lett.* **1996**, *77*, 3865−3868.
(27) Wang, Y.; Perdew, J. P. *Phys. Rev. B* **1991**, *44*, 13298−13307.
(28) Monkhorst, H. J.; Pack, J. D. *Phys. Rev. B* **1976**, *13*, 5188−5192.
(29) Suzuki, Y.; Morito, H.; Yamane, H. *J. Alloys Compd.* **2009**, *486*, 70−73.
(30) (a) von Schnering, H. G.; Curda, J.; Carillo-Cabrera, W.; Somer, M.; Peters, K. *Z. Kristallogr.* **1996**, *211*, 634. (b) Curda, J.; Carrillo Cabrera, W.; Schmeding, A.; Peters, K.; Somer, M.; von Schnering, H. G. *Z. Anorg. Allg. Chem.* **1997**, *623*, 929−936.
(31) Wiberg, N.; Finger, C. M. M.; Polborn, K. *Angew. Chem., Int. Ed.* **1993**, *32*, 1054−1056.
(32) Peterson, P. F.; Gutmann, M.; Proffen, Th.; Billinge, S. J. L. *J. Appl. Crystallogr.* **2000**, *33*, 1192−1192.
(33) Kanatzidis, M. G.; Billinge, S. J. L. *Chem. Commun.* **2004**, 749−760.
(34) Billinge, S. J. L.; Levin, I. *Science* **2007**, *316*, 561−565.
(35) Tucker, M. G.; Keen, D. A.; Dove, M. T.; Goodwin, A. L.; Hui, Q. *J. Phys.: Condens. Matter* **2007**, *19*, 335218.